Optical and NIR observations of the nearby type Ia supernova SN 2014J

Shubham Srivastav[1]⋆, J. P. Ninan[2]†, B. Kumar[1], G. C. Anupama[1], D. K. Sahu[1], D. K. Ojha[2], T. P. Prabhu[1]

[1]*Indian Institute of Astrophysics, II Block Koramangala, Bangalore 560 034, India*
[2]*Department of Astronomy and Astrophysics, Tata Institute of Fundamental Research, Homi Bhabha Road, Colaba, Mumbai - 400 005, India*

6 January 2016

ABSTRACT

Optical and NIR observations of the type Ia supernova SN 2014J in M82 are presented. The observed light curves are found to be similar to normal SNe Ia, with a decline rate parameter $\Delta m_{15}(B) = 1.08 \pm 0.03$. The supernova reached B-band maximum on JD 2456690.14, at an apparent magnitude $m_B(max) = 11.94$. The optical spectra show a red continuum with deep interstellar Na I absorption, but otherwise resemble those of normal SNe Ia. The Si II $\lambda6355$ feature indicates a velocity of $\sim 12\,000$ km s^{-1} at B-band maximum, which places SN 2014J at the border of the Normal Velocity and High Velocity group of SNe Ia. The velocity evolution of SN 2014J places it in the Low Velocity Gradient subclass, whereas the equivalent widths of Si II features near B-band maximum place it at the border of the Core Normal and Broad Line subclasses of SNe Ia. An analytic model fit to the bolometric light curve indicates that a total of ~ 1.3 M$_\odot$ was ejected in the explosion, and the ejected ^{56}Ni mass $M_{Ni} \sim 0.6$ M$_\odot$. The low [Fe III] $\lambda4701$ to [Fe II] $\lambda5200$ ratio in the nebular spectra of SN 2014J hints towards clumpiness in the ejecta. Optical broadband, linear polarimetric observations of SN 2014J obtained on four epochs indicate an almost constant polarization ($P_R \sim$2.7 per cent; $\theta \sim$37°), which suggests that the polarization signal is of interstellar origin.

Key words: supernova: general - supernovae: individual: SN 2014J - galaxies: individual: M82

1 INTRODUCTION

Type Ia supernovae (SNe Ia) are identified by the presence of a prominent Si II absorption trough near 6100 Å in their optical spectra (Filippenko 1997). SNe Ia constitute a remarkably homogeneous subclass, which makes them excellent standardizable candles for measuring cosmic distances (Riess et al. 1998; Perlmutter et al. 1999). SNe Ia are thought to be thermonuclear disruptions of accreting carbon-oxygen white dwarfs (WDs) in a close binary system (Hoyle & Fowler 1960; Woosley & Weaver 1986). Plausible progenitor systems for SNe Ia include the single degenerate (SD) scenario (Whelan & Iben 1973) where the companion is a main sequence or giant star, and the double degenerate (DD) scenario (Iben & Tutukov 1984; Webbink 1984) wherein the companion is also a WD (see Maoz, Mannucci & Nelemans 2014 for a recent review). The details of the explosion mechanism and the nature of the progenitor, however, still remain unclear. The wealth of recent data on SNe

Ia has revealed the inherent diversity within this class of objects. While the majority ($\sim 70\%$) of SNe Ia fall under the "normal" category, sub-luminous 1991bg-like objects make up $\sim 18\%$, whereas over-luminous 1991T-like events and peculiar 2002cx-like events constitute the remaining 12% (Li et al. 2011).

The uncertainty in the amount of extinction suffered by SNe Ia in their host galaxy environment is a significant obstacle in using them effectively as cosmological probes. Highly reddened SNe Ia tend to show unusually low values of $R_V \lesssim 2$ (Nobili & Goobar 2008; Phillips et al. 2013), eg. SN 1999cl (Krisciunas et al. 2006), SN2002cv (Elias-Rosa et al. 2008), SN 2003cg (Elias-Rosa et al. 2006) and 2006X (Wang et al. 2008); as opposed to the average Galactic value of $R_V = 3.1$. The observational evidence suggests that SNe Ia generally exhibit very weak continuum polarization ($P \lesssim 0.3$ per cent) but a moderate level of line polarization up to a few per cent (see, Wang, Wheeler & Höflich 1997; Wang et al. 2003, 2006; Leonard et al. 2005; Chornock et al. 2006; Wang & Wheeler 2008; Patat et al. 2009; Smith et al. 2011; Maund et al. 2013, and references therein). The continuum and line polarization depend upon the geometry of explo-

⋆ E-mail : ssrivastav@iiap.res.in
† E-mail : ninan@tifr.res.in

sion and distribution of matter around the SN, respectively (Wang & Wheeler 2008). Therefore, study of polarization properties can provide information on asymmetry and orientation and also shed light on the time-varying behaviour of the SN ejecta. Generally, a significant level of line and continuum polarization tends to be detected in these events at early times (pre or near maximum light), decreasing at later epochs (although there are exceptions, for example see Zelaya et al. 2013).

SN 2014J was serendipitously discovered by Fossey et al. (2014) on 2014 January 21, in the nearby galaxy M82. The discovery prompted an international multi-wavelength observational effort, spanning radio to γ-ray observations. At a distance of only ~ 3.5 Mpc, SN 2014J is among the nearest SNe Ia ever observed and thus provides an excellent opportunity to study in detail the properties of the progenitor and the nature of absorbing dust along the line of sight.

Pre-discovery observations were reported from the Katzman Automatic Imaging Telescope (KAIT) as part of the Lick Observatory Supernova Search (LOSS) by Zheng et al. (2014), who also constrained the time of first-light between January 14.54 and 14.96 UT, with January 14.75 UT as the best estimate. Using high cadence pre-explosion data obtained by the Kilodegree Extremely Little Telescope (KELT), Goobar et al. (2015) report an explosion date of January 14.54 ± 0.3 UT, 5 hours earlier than that reported by Zheng et al. (2014).

Several detailed studies spanning a wide range of the electromagnetic spectrum have been published on SN 2014J. Goobar et al. (2014) presented early optical and near-infrared (NIR) observations and noted the presence of high velocity features of Si II and Ca II in the optical spectra and a best-fit value of $R_V = 1.4 \pm 0.15$ to explain the observations. Amanullah et al. (2014) presented ultraviolet (UV) to NIR photometry of SN 2014J up to ~ 40 days past B-band maximum and inferred best-fit reddening parameter values of $E(B-V)_{true} \sim 1.3$ and $R_V \sim 1.4$ for a Galactic extinction law. The results of Amanullah et al. (2014) were also found to be consistent with power-law extinction which was invoked by Goobar (2008) to account for extinction caused by multiple scattering. Using multi-band photometry spanning UV to NIR, Foley et al. (2014) reported similar reddening parameters of $E(B - V)_{true} \sim 1.2$ and $R_V \sim 1.4$. However, a two component model involving a typical dust component ($R_V \sim 2.5$) and a circumstellar scattering component provided a better fit to the data (Foley et al. 2014). Further, Gao et al. (2015) used dust models comprising graphite and silicate components in order to model the color excess toward SN 2014J and inferred $E(B - V)_{true} \sim 1.1$ and $R_V \sim 1.7$, consistent with the results of Amanullah et al. (2014) and Foley et al. (2014). Using *Swift*-UVOT data for SN 2014J, Brown et al. (2015) concurred with the low value of R_V derived by previous authors, but argued for an interstellar origin for the extinction rather than circumstellar. Although C II is not detected in the early optical spectra (Goobar et al. 2014), Marion et al. (2015) reported detection of the C I 1.0693 μm feature in their NIR spectra. Jack et al. (2015) presented a time series of high resolution spectra of SN 2014J and confirmed the presence of interstellar medium (ISM) features and diffuse interstellar bands (DIBs) in the spectra. Kawabata et al. (2014) and Patat et al. (2015) present linear polarimetric observations of SN 2014J, which

highlight the peculiar properties of dust in M82 and argue that the major contribution to extinction comes from interstellar dust rather than circumstellar matter (CSM). Crotts (2015) report detection of light echoes from SN 2014J, the most prominent ones originating at distances of 80 pc and 330 pc from the SN. An early detection of γ-ray lines from SN 2014J was reported by Diehl et al. (2014), while subsequent observations of γ-ray emission due to ^{56}Co were presented by Churazov et al. (2014); Diehl et al. (2015).

Various lines of evidence seem to favor the DD progenitor scenario for SN 2014J. Using pre-explosion archival *HST* images, Kelly et al. (2014) ruled out a bright red giant companion as the donor. The non-detection of radio (Pérez-Torres et al. 2014) and X-ray emission (Margutti et al. 2014) also rule out a majority of the parameter space occupied by SD models. Lundqvist et al. (2015) failed to find traces of accreted material from a non-degenerate companion in nebular spectra, strengthening the case for the DD scenario for SN 2014J.

We present in this paper the results of extensive monitoring of SN 2014J in optical and NIR bands undertaken at the Indian Astronomical Observatory (IAO) using the 2-m Himalayan Chandra Telescope (HCT). Also presented are four epochs of broadband polarimetric observations obtained using the ARIES Imaging Polarimeter mounted at the 1-m Sampurnanand Telescope (ST) at Manora Peak, Nainital.

2 OBSERVATIONS AND REDUCTION

2.1 Optical Photometry

Photometric observations of SN 2014J commenced on 2014 January 24, ~ 8 days before B-band maximum, using the 2-m Himalayan Chandra Telescope at the Indian Astronomical Observatory at Hanle, and continued till 2014 October 28. The observations were made with the Himalayan Faint Object Spectrograph Camera (HFOSC). The SITe CCD available with the HFOSC has an imaging area of 2K $\times$ 4K pixels, of which the central unvignetted 2K $\times$ 2K area was used for imaging. The field of view in imaging mode is 10 $\times$ 10 arcmin^2, with an image scale of 0.296 arcsec pixel^{-1}. The SN was imaged in the Bessell $UBVRI$ filters available with the HFOSC. Landolt standard field PG0918+029 (Landolt 1992) was observed under photometric conditions on the nights of 2014 January 30, February 24 and February 26 for photometric calibration of the supernova field.

Data reduction was performed in the standard manner using various packages available with the Image Reduction and Analysis Facility (IRAF[1]). Aperture photometry was performed on the standard stars at two apertures - an aperture close to the FWHM of the stellar profile, and another aperture of around 4 times the FWHM of the stellar profile. Aperture corrections were calculated as the difference in magnitude for the two apertures. Average aperture corrections were calculated using all the stars in the standard field. Average extinction coefficients for the site (Stalin et al.

2008) were used in order to account for atmospheric extinction, and average values of the color terms for the HFOSC system were used to arrive at the photometric solutions. The solutions thus obtained were used to calibrate local standards in the supernova field, observed on the same night as the standard fields. The local standards were thereafter used to calibrate the supernova magnitudes. The field for SN 2014J is shown in Figure 1, and the magnitudes of the secondary standards are listed in Table 1.

The magnitudes of the supernova and the secondary standards were evaluated using point-spread function (PSF) fitting, with a fitting radius close to the FWHM of the stellar profile. Nightly photometric zero points were estimated using the local secondary standards and the supernova magnitudes were evaluated differentially.

Since SN 2014J exploded in the interior of the bright starburst galaxy M82, there is significant contamination by the host galaxy in the late phase optical photometry. In order to subtract the host galaxy contribution, we used pre-explosion Sloan Digital Sky Survey (SDSS) *ugriz* images of M82 as templates. In order to transform the images from *ugriz* to *BVRI* filter system, we used the transformations prescribed by Lupton (2005)[2]. The transformed SDSS images were then used as templates for host galaxy subtraction.

In order to check the robustness of this method, we applied the template subtraction to images obtained near the epoch of maximum brightness, where the host galaxy contamination is expected to be minimal. The magnitudes obtained using template subtraction were seen to show excellent agreement with those obtained using PSF photometry near epochs of maximum brightness. The magnitudes calculated using the above two methods indicate host galaxy contribution in the estimated SN magnitudes beyond ~ 60 days since B-band maximum. Hence, beyond this epoch, we use the template-subtracted magnitudes.

Table 2 summarizes the optical $UBVRI$ photometric observations and also lists the estimated magnitudes of SN 2014J.

2.2 NIR Photometry

NIR photometric observations of SN 2014J were carried out in J, H and K_S bands using the TIFR Near Infrared Spectrometer and Imager (TIRSPEC) mounted on HCT. TIRSPEC's detector is 1024×1024 Hawaii-1 PACE[3] (HgCdTe) array. It has a pixel size of 18 μm and a field of view (FoV) of $\sim 5 \times 5$ arcmin^2. Broadband filters used for observations were J (λ_{center}= 1.25 μm, $\Delta\lambda$= 0.16 μm), H (λ_{center}= 1.635 μm, $\Delta\lambda$= 0.29 μm) and K_S (λ_{center}= 2.145 μm, $\Delta\lambda$= 0.31 μm) (Mauna Kea Observatories Near-Infrared filter system). Further details of TIRSPEC are available in Ninan et al. (2014) and Ojha et al. (2012). A total of 17 nights of NIR photometric observations were obtained between 2014 January 24 and 2014 April 30 (Table 2).

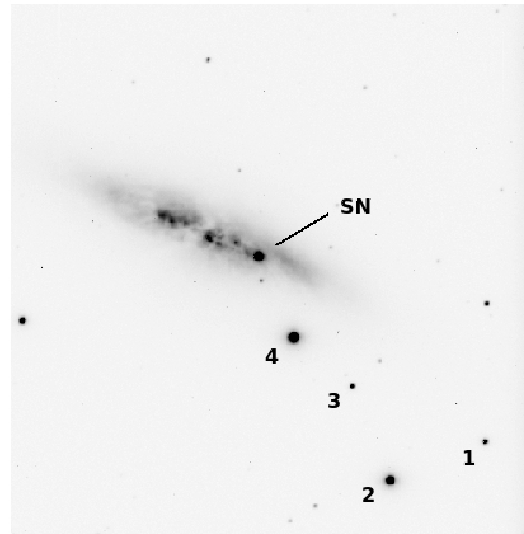Observations were carried out by pointing the telescope

Figure 1. Identification chart for SN 2014J. North is up and East is to the left. The field of view is $10' \times 10'$. Local standards are marked.

at 5 dither positions with 15″ step size. For generating a master sky frame, a separate sky region was also observed with same exposure and dither pattern immediately after each SN observation. A dark patch with no extended sources, 400″north of SN 2014J was chosen as the sky region. Data reduction was done using TIRSPEC photometry pipeline (Ninan et al. 2014). The pipeline subtracts dark current for the equivalent exposure, and uses twilight flats of the same night for flat correction of data. Aperture photometry as well as PSF photometry were found to have significant contamination from the non-uniform background of the host galaxy. Hence, 2MASS archive image of the galaxy was used as template and the galaxy background image was subtracted before aperture photometry. For aperture photometry, an aperture of 3 times FWHM was used. The uniform background sky was estimated from a ring outside the aperture radius with a width of 4.5″. 2MASS magnitudes of secondary standards in the field were used for magnitude calibration and color correction. Table 2 summarizes the JHK_s magnitudes of SN 2014J.

2.3 Optical Spectroscopy

Optical spectroscopic observations of SN 2014J were made during 2014 January 24 to 2015 January 18, using grisms Gr7 (3500-7800 Å) and Gr8 (5200-9250 Å) available with the HFOSC. The details of the spectroscopic observations are summarized in Table 3. Lamp spectra of FeAr and FeNe were used for wavelength calibration. The spectra were extracted in the standard manner. Night sky emission lines $\lambda5577$, $\lambda6300$ and $\lambda6363$ were used to check the wavelength calibration and spectra were shifted wherever necessary. Spectra of spectrophotometric standards were observed in order to deduce instrumental response curves for flux calibration. For those nights where standard star observations were not available, the response curves obtained during nearby nights were used. The flux calibrated spectra in grisms Gr7 and Gr8 were combined with appropriate scaling to give a sin-

---

[2] https://www.sdss3.org/dr8/algorithms/
sdssUBVRITransform.php#Lupton2005
[3] HgCdTe Astronomy Wide Area Infrared Imager -1, Producible Alternative to CdTe for Epitaxy

Table 1. $UBVRI$ Magnitudes of secondary standards in the field of SN 2014J

ID	U	B	V	R	I
1	13.755 ± 0.010	13.912 ± 0.003	13.407 ± 0.002	13.095 ± 0.008	12.769 ± 0.011
2	12.113 ± 0.006	11.553 ± 0.007	10.715 ± 0.005	10.264 ± 0.001	9.871 ± 0.009
3	14.182 ± 0.010	14.351 ± 0.006	13.790 ± 0.005	13.458 ± 0.008	13.118 ± 0.004
4	10.761 ± 0.007	10.654 ± 0.004	10.052 ± 0.005	9.739 ± 0.026	9.452 ± 0.007

gle spectrum, which was brought to an absolute flux scale using the broadband $UBVRI$ photometric magnitudes. The spectra were corrected for redshift of the host galaxy. The telluric lines have not been removed from the spectra.

2.4 NIR Spectroscopy

NIR spectroscopic monitoring of SN 2014J from 1.02 μm to 2.35 μm was carried out using TIRSPEC. Spectroscopic observations were carried out using 1.97″ wide long slit with a resolution of R ∼ 1200. Complete spectral range was covered in separate single order mode observations of Y, J, H and K orders. Source spectrum was taken at least in two dither positions along the slit. Argon lamp spectrum for wavelength calibration and Tungsten lamp for smooth continuum flat correction were taken immediately after each observation before moving any of the optics elements like grism or slit. The nearby bright telluric standard star Alp Leo was also observed in exactly the same configuration for telluric line correction immediately after SN 2014J observations. The log of NIR observations is listed in Table 3.

Spectroscopic data were reduced using TIRSPEC spectroscopy pipeline. Wavelength calibrated spectra were divided using the telluric standard star spectra, and finally multiplied by a blackbody curve with a temperature of 11 800 K (telluric standard star temperature). The final spectra were flux calibrated using the magnitudes obtained from our photometric observations. Y band spectra were separately calibrated by interpolating fluxes in I and J bands.

2.5 Broadband Polarimetry

Broadband linear polarimetric observations of SN 2014J were made during four nights, using the ARIES Imaging Polarimeter (AIMPOL, Rautela, Joshi, & Pandey 2004) mounted at the Cassegrain focus of the 104-cm Sampurnanand telescope (ST) at Manora Peak, Nainital. On the first epoch, observations were obtained in the VRI bands, but only in the R-band thereafter. The log of polarimetric observations is given in Table 4.

The polarimeter consists of a half-wave plate (HWP) modulator and a Wollaston prism beam-splitter. The Wollaston prism analyzer is placed at the backend of the telescope beam path in order to produce ordinary and extraordinary beams in slightly different directions separated by 28 pixels along the north-south direction on the sky plane. A focal reducer (85 mm, f/1.8) is placed between the Wollaston prism and the CCD camera. The AIMPOL camera is composed of 1024 pixels × 1024 pixels. Each pixel corresponds to 1.73 arcsec, and the FoV is ∼8 arcmin in diameter on

the sky. The FWHM of the stellar images varies from 2 to 3 pixels. At each position of the half-wave plate (0°, 22.5°, 45° and 67.5°), multiple sets of frames were obtained.

Fluxes of ordinary (I_o) and extra-ordinary (I_e) beams of the SN were extracted by standard aperture photometry after pre-processing using IRAF. The detailed procedures used to estimate the polarization and polarization angles for the target objects can be found in Ramaprakash et al. (1998) and Rautela, Joshi & Pandey (2004).

To correct our measurements for the zero-point polarization angle, polarized standard stars (BD 59389, HD 19820, HD 155197, HD 25443, HD 16056, HD 154445 and HD 25443; from Schmidt, Elston & Lupie 1992) were observed on each night. The difference between the observed and standard values were applied to the SN. The instrumental polarization of AIMPOL on the 104 cm ST has been characterized for different projects and generally found to be ∼0.1 per cent (e.g., Rautela, Joshi & Pandey 2004; Pandey et al. 2009; Eswaraiah et al. 2011, 2012; Kumar et al. 2014, and references therein). The SN polarization has been calibrated by applying this offset value. The estimated SN polarization parameters are listed in Table 4.

3 OPTICAL AND NIR LIGHT CURVES

SN 2014J was observed in the $UBVRI$ bands from −8d to +269d, and in the NIR JHK_s bands from −8d to +88d since B-band maximum, which occurred on JD 2456690.14± 0.5 at an apparent magnitude of 11.94 ± 0.02. The optical and NIR light curves of SN 2014J are shown in Figures 2 and 3, respectively. The photometric properties of SN 2014J extracted from the light curves are summarized in Table 5.

SN 2014J suffers an unusually large amount of extinction in its host environment. In addition to a single component dust model with low R_V, Foley et al. (2014) had also invoked a two component dust model which consists of a typical dust component along with a Large Magellanic Cloud-like dust component in the circumstellar environment of SN 2014J in order to explain the observations. However, polarization studies seem to rule out the presence of a CSM (Kawabata et al. 2014; Patat et al. 2015). Brown et al. (2015) also attribute most of the observed extinction to dust of interstellar rather than circumstellar origin. Thus, in order to account for host extinction, we favor the single dust component model with $E(B-V)_{true} = 1.24 \pm 0.10$ and $R_V = 1.44 \pm 0.06$ (Foley et al. 2014) for a standard CCM reddening law (Cardelli, Clayton & Mathis 1989), as modified by O'Donnell (1994).

The observed decline rate parameter, $\Delta m_{15}(B)_{obs} = 0.96 \pm 0.03$. However, the large amount of reddening effectively shifts the wavelength being sampled towards the red.

Table 2. Optical and NIR photometry of SN 2014J

Date (yyyy/mm/dd)	JD (245 6000+)	Phase* (days)	U	B	V	R	I	J	H	K_s
2014/01/24	682.43	−7.71	12.75 ± 0.01	12.45 ± 0.02	11.12 ± 0.02	10.49 ± 0.02	10.09 ± 0.02	9.55	9.60	9.48
2014/01/25	683.49	−6.65	12.62 ± 0.01	12.30 ± 0.02	10.98 ± 0.01	10.39 ± 0.01	9.99 ± 0.01			
2014/01/26	684.49	−5.65	12.51 ± 0.02	12.20 ± 0.01	10.87 ± 0.01	10.31 ± 0.01	9.95 ± 0.02			
2014/01/27	685.50	−4.64	12.46 ± 0.02	12.10 ± 0.01	10.78 ± 0.01	10.25 ± 0.01	9.86 ± 0.02			
2014/01/28	686.24	−3.90	12.41 ± 0.01	12.07 ± 0.02	10.73 ± 0.02	10.21 ± 0.01	9.85 ± 0.01			
2014/01/29	687.36	−2.78	12.36 ± 0.01	12.01 ± 0.02	10.65 ± 0.01	10.13 ± 0.02	9.82 ± 0.01	9.35	9.51	9.24
2014/01/30	688.38	−1.76	12.36 ± 0.02	11.96 ± 0.01	10.61 ± 0.02	10.11 ± 0.02	9.81 ± 0.02	9.35	9.54	9.33
2014/01/31	689.37	−0.77	12.34 ± 0.01	11.94 ± 0.01	10.56 ± 0.01	10.13 ± 0.01	9.83 ± 0.02	9.43	9.62	9.36
2014/02/01	690.41	+0.27	12.38 ± 0.01	11.94 ± 0.01	10.55 ± 0.01	10.10 ± 0.01	9.85 ± 0.01			
2014/02/02	691.06	+0.92	12.41 ± 0.01	11.95 ± 0.01	10.54 ± 0.02	10.11 ± 0.02	9.86 ± 0.02			
2014/02/03	692.29	+2.15			10.56 ± 0.01	10.14 ± 0.01	9.92 ± 0.02			
2014/02/05	694.17	+4.03	12.56 ± 0.01	12.03 ± 0.01	10.57 ± 0.01	10.15 ± 0.01	9.97 ± 0.01			
2014/02/07	696.42	+6.28	12.69 ± 0.01	12.14 ± 0.01	10.61 ± 0.01	10.21 ± 0.02	10.05 ± 0.02			
2014/02/09	698.46	+8.32	12.84 ± 0.01	12.28 ± 0.02	10.72 ± 0.02	10.34 ± 0.01	10.17 ± 0.01			
2014/02/11	700.28	+10.14	13.00 ± 0.01	12.43 ± 0.01	10.83 ± 0.01	10.47 ± 0.02	10.30 ± 0.01	10.83	10.08	9.74
2014/02/12	701.34	+11.20	13.11 ± 0.01	12.52 ± 0.01	10.89 ± 0.01	10.54 ± 0.01	10.34 ± 0.01	11.08	10.02	9.80
2014/02/16	705.34	+15.20	13.58 ± 0.01	12.92 ± 0.02	11.13 ± 0.004	10.78 ± 0.02	10.41 ± 0.01			
2014/02/17	706.15	+16.01	13.68 ± 0.02	12.99 ± 0.01	11.18 ± 0.01	10.78 ± 0.01	10.39 ± 0.02			
2014/02/18	707.09	+16.95	13.82 ± 0.01	13.13 ± 0.01	11.24 ± 0.01	10.80 ± 0.01	10.38 ± 0.01			
2014/02/18	707.49	+17.35		13.17 ± 0.01	11.26 ± 0.01	10.80 ± 0.02	10.39± 0.01			
2014/02/19	708.38	+18.24	13.98 ± 0.01	13.26 ± 0.01	11.27 ± 0.01	10.82 ± 0.01	10.35± 0.01			
2014/02/20	709.31	+19.17	14.11 ± 0.02	13.37 ± 0.01	11.32 ± 0.01	10.81 ± 0.02	10.34 ± 0.01			
2014/02/21	710.24	+20.10		13.45 ± 0.02	11.34 ± 0.02	10.80 ± 0.01	10.30 ± 0.01			
2014/02/23	712.34	+22.20		13.67 ± 0.01	11.39 ± 0.01	10.80 ± 0.01	10.24 ± 0.01	11.24	9.79	9.66
2014/02/24	713.32	+23.18	14.58 ± 0.01	13.76 ± 0.01	11.43 ± 0.01	10.79 ± 0.01	10.22 ± 0.01			
2014/02/25	714.32	+24.18	14.69 ± 0.01	13.84 ± 0.01	11.47 ± 0.01	10.79 ± 0.02	10.20 ± 0.01	11.19	9.70	9.66
2014/02/26	715.32	+25.18	14.79 ± 0.01	13.93 ± 0.01	11.51 ± 0.02	10.82 ± 0.01	10.19 ± 0.01			
2014/02/27	716.30	+26.16		14.05 ± 0.01	11.55 ± 0.02	10.84 ± 0.01	10.18 ± 0.01	10.93	9.66	9.56
2014/02/28	717.27	+27.13			11.60 ± 0.01	10.86 ± 0.01	10.18 ± 0.01			
2014/03/01	718.39	+28.25	15.02 ± 0.02	14.20 ± 0.01	11.65 ± 0.01	10.91 ± 0.02	10.17 ± 0.01			
2014/03/02	719.37	+29.23						10.74	9.69	9.61
2014/03/03	720.31	+30.17	15.16 ± 0.01	14.34 ± 0.01	11.73 ± 0.01	10.96 ± 0.01	10.20 ± 0.02	10.66	9.70	9.68
2014/03/04	721.33	+31.19	15.22 ± 0.01	14.40 ± 0.01	11.80 ± 0.01	11.00 ± 0.01	10.20 ± 0.01	10.66	9.69	9.73
2014/03/05	722.28	+32.14	15.31 ± 0.02	14.47 ± 0.02	11.87 ± 0.01	11.05 ± 0.01	10.21 ± 0.03	10.59	9.78	9.75
2014/03/06	723.30	+33.16	15.34 ± 0.02	14.52 ± 0.01	11.93 ± 0.01	11.13 ± 0.01	10.29 ± 0.02	10.65	9.79	9.80
2014/03/09	726.32	+36.18	15.49 ± 0.01	14.68 ± 0.01	12.11 ± 0.01	11.34 ± 0.01	10.54 ± 0.02			
2014/03/12	729.29	+39.15	15.60 ± 0.01	14.81 ± 0.01	12.29 ± 0.01	11.53 ± 0.01	10.78 ± 0.02			
2014/03/13	730.25	+40.11	15.63 ± 0.02	14.83 ± 0.01	12.30 ± 0.01	11.60 ± 0.02	10.81 ± 0.01			
2014/03/14	731.23	+41.09		14.88 ± 0.02	12.34 ± 0.01	11.61 ± 0.02	10.86 ± 0.02	11.40	10.33	10.42
2014/03/16	733.38	+43.24	15.71 ± 0.02	14.90 ± 0.01	12.42 ± 0.01	11.70 ± 0.01	10.96 ± 0.01			
2014/03/18	735.24	+45.10	15.72 ± 0.02	14.94 ± 0.01	12.48 ± 0.01	11.80 ± 0.02	11.09 ± 0.02			
2014/03/21	738.49	+48.35		14.97 ± 0.01	12.60 ± 0.01	11.96 ± 0.02	11.29 ± 0.02			
2014/03/25	742.24	+52.10	15.83 ± 0.01	15.03 ± 0.01	12.67 ± 0.01	12.04 ± 0.01	11.40 ± 0.02			
2014/03/27	744.33	+54.19		15.05 ± 0.02	12.74 ± 0.01	12.13 ± 0.01	11.50 ± 0.02			
2014/04/03	751.23	+61.09		15.16 ± 0.02	12.95 ± 0.02	12.37 ± 0.01	11.85 ± 0.03	12.89	11.30	11.28
2014/04/11	759.18	+69.04	16.12 ± 0.03	15.26 ± 0.02	13.21 ± 0.01	12.63 ± 0.02	12.17 ± 0.01			
2014/04/17	765.37	+75.23		15.31 ± 0.01	13.33 ± 0.01	12.81 ± 0.01	12.30 ± 0.02			
2014/04/27	775.34	+85.20		15.46 ± 0.01	13.60 ± 0.01	13.14 ± 0.02	12.78 ± 0.02			
2014/04/30	778.16	+88.02		15.50 ± 0.01	13.68 ± 0.01	13.18 ± 0.01	12.86 ± 0.02	15.06	12.75	12.40
2014/05/03	781.31	+91.17	16.62 ± 0.02	15.51 ± 0.02	13.75 ± 0.01	13.29 ± 0.01	12.98 ± 0.03			
2014/05/07	785.25	+95.11		15.62 ± 0.01	13.88 ± 0.02	13.47 ± 0.03	13.15 ± 0.03			
2014/05/27	805.26	+115.12	17.20 ± 0.02	15.87 ± 0.05	14.39 ± 0.01	14.03 ± 0.02	13.80 ± 0.03			
2014/06/04	813.24	+123.10		16.03 ± 0.02	14.57 ± 0.04	14.24 ± 0.02	14.00 ± 0.02			
2014/06/16	825.13	+134.99		16.22 ± 0.02	14.88 ± 0.04	14.55 ± 0.04	14.23 ± 0.04			
2014/07/05	844.17	+154.03		16.53 ± 0.02	15.29 ± 0.02	14.98 ± 0.01	14.60 ± 0.03			
2014/07/21	860.17	+170.03		16.75 ± 0.02	15.57 ± 0.02	15.35 ± 0.02	14.91 ± 0.05			
2014/09/27	928.43	+238.29		17.67 ± 0.02	16.59 ± 0.04	16.27 ± 0.04	15.71 ± 0.02			
2014/10/28	959.46	+269.32		18.08 ± 0.04	16.99 ± 0.03	17.01 ± 0.03	16.08 ± 0.03			

*time since B-band max (JD 2456690.14)

The reddening-corrected decline rate parameter defined by Phillips et al. (1999) is given by

$$\Delta m_{15}(B)_{true} \simeq \Delta m_{15}(B)_{true} + 0.1 E(B-V)_{true}$$

For $E(B-V)_{true} = 1.24$, we get $\Delta m_{15}(B)_{true} \simeq 1.08 \pm 0.03$, which is consistent with the estimates of Foley et al. (2014); Ashall et al. (2014); Tsvetkov et al. (2014); Marion et al. (2015).

Like in other normal SNe Ia, the light curves in the redder bands peak before B-band maximum. The optical $BVRI$ light curves of SN 2014J are compared with those of other normal SNe Ia like SN 2011fe (Richmond & Smith 2012), 2005cf (Pastorello et al. 2007) and 2003du (Anupama, Sahu & Jose 2005) in Figure 4. The SN magnitudes were normalized to the peak magnitudes in each filter and shifted in time to correspond to the epoch of B-band maximum for SN

Table 3. Log of spectroscopic observations of SN 2014J

Date (yyyy/mm/dd)	JD 245 6000+	Phase* (days)	Range (Å)
2014/01/24	682.43	−7.71	3500-7800; 5200-9250
2014/01/25	683.49	−6.65	3500-7800; 5200-9250
2014/01/26	684.49	−5.65	3500-7800; 5200-9250
2014/01/27	685.50	−4.64	3500-7800; 5200-9250
2014/01/28	686.24	−3.90	3500-7800; 5200-9250
2014/01/29	687.36	−2.78	3500-7800; 5200-9250; $YJHK$
2014/01/31	689.37	−0.77	3500-7800; 5200-9250
2014/02/01	690.41	+0.27	3500-7800; 5200-9250; JK
2014/02/02	691.06	+0.92	3500-7800; 5200-9250
2014/02/07	696.42	+6.28	3500-7800; 5200-9250
2014/02/11	700.30	+10.16	3500-7800; 5200-9250; $YJHK$
2014/02/12	701.36	+11.22	3500-7800; 5200-9250; YJH
2014/02/18	707.09	+16.95	3500-7800; 5200-9250
2014/02/26	715.32	+25.18	3500-7800; 5200-9250
2014/03/05	722.28	+32.14	3500-7800; 5200-9250
2014/03/13	730.25	+40.11	3500-7800; 5200-9250
2014/03/18	735.24	+45.10	3500-7800; 5200-9250
2014/03/28	745.46	+55.32	3500-7800; 5200-9250
2014/04/03	751.23	+61.09	3500-7800; 5200-9250
2014/04/30	778.16	+88.02	3500-7800; 5200-9250
2014/07/05	844.17	+154.03	3500-7800; 5200-9250
2014/10/28	959.46	+269.32	3500-7800; 5200-9250
2015/01/18	1041.24	+351.09	3500-7800; 5200-9250

*time since B-band max (JD 2456690.14)

Table 4. Log of polarimetric observations and estimated polarization parameters of SN 2014J.

UT Date (yyyy/mm/dd)	JD 2456000+	Phase* (days)	Filter	$P \pm \sigma_P$ (per cent)	$\theta \pm \sigma_\theta$ (°)
2014/01/24	682.37	−7.77	V	3.77 ± 0.02	39.28 ± 1.43
			R	2.64 ± 0.06	34.85 ± 1.87
			I	1.59 ± 0.09	38.95 ± 1.73
2014/02/05	694.21	+4.07	R	2.64 ± 0.05	38.24 ± 1.13
2014/03/06	723.18	+33.04	R	2.67 ± 0.04	39.26 ± 1.45
2014/03/30	747.35	+57.21	R	2.70 ± 0.04	33.72 ± 2.26

*time since B-band max (JD 2456690.14)

2014J. The $BVRI$ light curves of SN 2014J are remarkably similar to the other SNe Ia used for comparison.

4 POLARIZATION RESULTS

The observed polarization parameters of SN 2014J in different optical bands are shown in Figure 5. Kawabata et al. (2014, hereafter K14) have used broadband optical and NIR polarimetric observations of SN 2014J obtained at five epochs to study the dust properties of M82 in the SN region. In general, our estimated results are consistent with K14 i.e. the polarization angle in R-band remains almost constant (average value $36.52° \pm 3.46°$) which indicates alignment with local spiral structure of M82 (Greaves et al. 2000). However, the average degree of polarization (in R-band) found in the present study is slightly higher than the estimated value of K14. Although our observations in V and I bands are restricted to a single epoch, the estimated polarization parameters in both studies are similar. In order to examine the

simultaneous behaviour of the polarization and the polarization angle of SN 2014J, the observed Q-U Stokes parameters are plotted in Figure 6, where each number represents a data pair of the Q-U vector in R-band. The limited data points, although indicative of these vectors being aligned along a line (within observational uncertainties), are not sufficient to draw conclusions on the geometry of the ejecta.

It is interesting to note that the photometric properties of SN 2014J show similarity with SN 2011fe, SN 2005cf and SN 2003du (see Sec 3). These SNe Ia showed relatively low host galaxy extinction (c.f. Anupama, Sahu & Jose 2005; Pastorello et al. 2007; Patat et al. 2013). Smith et al. (2011) presented multi-epoch spectropolarimetric observations of SN 2011fe and inferred asymmetry in the photosphere with intrinsic continuum polarization between $0.2 - 0.4$ per cent. Additionally, they found a shift in polarization angle of $90°$ during the follow-up period (up to 43d after the explosion), implying a time-dependent large-scale asymmetry in the explosion. In a similar study of SN 2003du, Leonard et al.
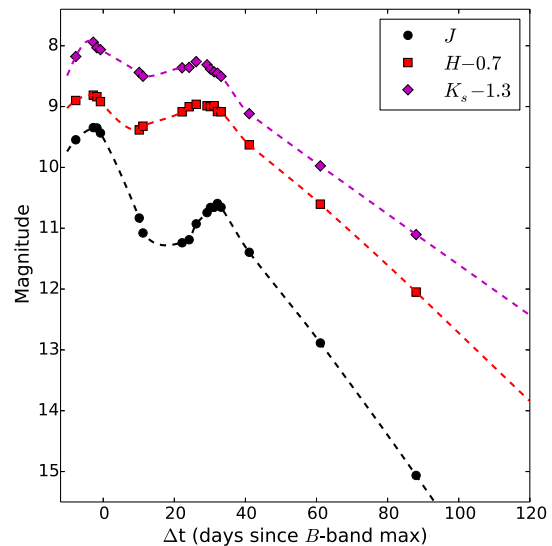
Table 5. Photometric properties of SN 2014J

Band	JD (Max) 245 6000+	m_λ^{max}	M_λ^{max}	$\Delta m_{15}(\lambda)$	Decline Rate (50-100d) mag $(100d)^{-1}$	Decline Rate (100-250d) mag $(100d)^{-1}$
U	689.33	12.34	-19.70	1.11	2.08	-
B	690.14	11.93	-19.09	1.08	1.38	1.43
V	690.96	10.54	-19.13	0.62	2.76	1.82
R	689.60	10.10	-18.84	0.64	3.24	1.93
I	688.24	9.81	-18.43	0.58	3.98	1.68
J	687.81	9.34	-18.68	1.83	8.04	-
H	687.21	9.51	-18.41	0.49	5.32	-
K_s	686.41	9.22	-18.62	0.58	4.20	-
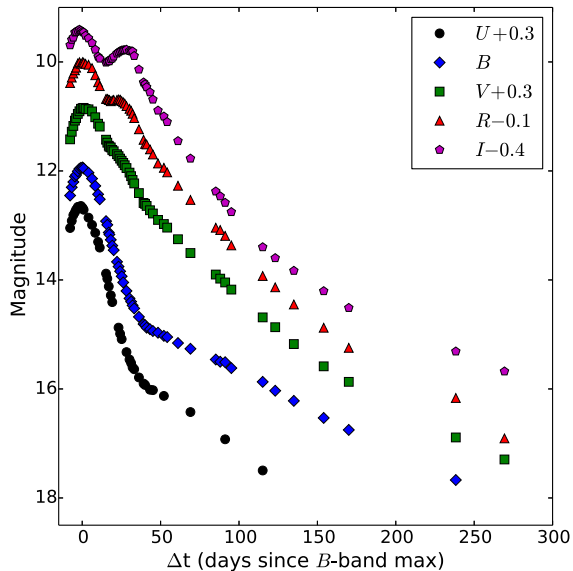
Figure 2. Optical $UBVRI$ light curves of SN 2014J. The magnitudes past +60d are derived using template subtraction. The typical errors on the magnitudes are smaller than the symbol size.

Figure 3. NIR JHK_s light curves of SN 2014J.

(2005) estimated an intrinsic polarization of 0.3 per cent and predicted clumps in the ejecta.

Based on the data set presented here, it is not possible to draw a firm conclusion about the SN ejecta and intrinsic polarization properties of SN 2014J. However, the results show consistency with that of K14 and Patat et al. (2015). As stated previously, there is no significant variation in the polarization parameters of this event. Nonetheless, as discussed by Maeda et al. (2015), it is possible that a combination of phenomena (e.g. multiple scattering and ISM absorption) is responsible for such an abnormally high observed degree of polarization for SN 2014J. The near constant polarization in R-band over nearly 70 days suggests that the polarization signal was of interstellar origin and the SN was likely minimally polarized. Using high resolution spectra, Ritchey et al. (2015) concluded a wide range of physical/environmental conditions in the ISM of M82. The light echo properties of this event also indicate a complex structure for the interstellar dust in the host galaxy (Crotts 2015).

5 BOLOMETRIC LIGHT CURVE

The quasi-bolometric light curve of SN 2014J was constructed using the broadband $UBVRIJHK_s$ photometry described in the previous section. The broadband optical and NIR magnitudes were corrected for extinction assuming $E(B - V)_{true} = 1.24$ for a Galactic extinction law with $R_V = 1.44$, which are the best-fit values obtained by Foley et al. (2014). Following Foley et al. (2014), we use $E(B - V)_{MW} = 0.05$ to account for Milky Way reddening. The extinction-corrected magnitudes were then converted to monochromatic fluxes using the zero points from Bessell, Castelli & Plez (1998). A spline curve was then fit through the monochromatic fluxes and the resulting curve was integrated under appropriate limits of wavelength as determined from the filter response curves, to yield the quasi-bolometric flux for the particular epoch. In order to estimate the UV contribution to the bolometric flux, we use the *HST* spectra presented by Foley et al. (2014). It may be noted that a significant portion of the HST UV spectra at the blue end had to be rejected owing to poor signal. The UV contribution estimated here for SN 2014J might thus be treated as a lower limit. We estimate that the UV contribution falls
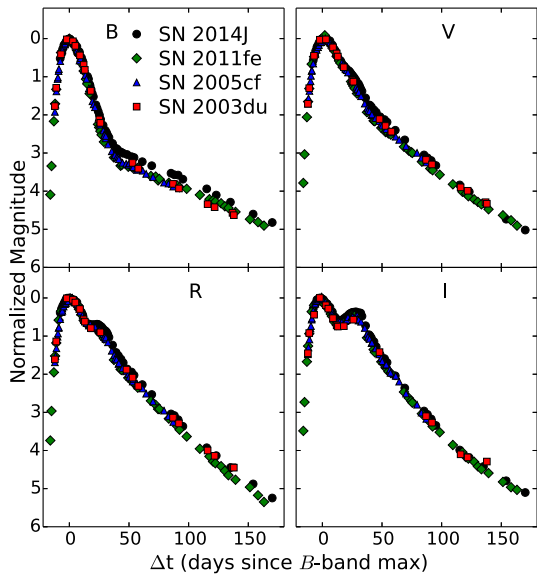
Figure 4. Comparison of $BVRI$ light curves of SN 2014J with SN 2011fe, SN 2005cf and SN 2003du. The light curves of the SNe used for comparison have been shifted as described in the text.
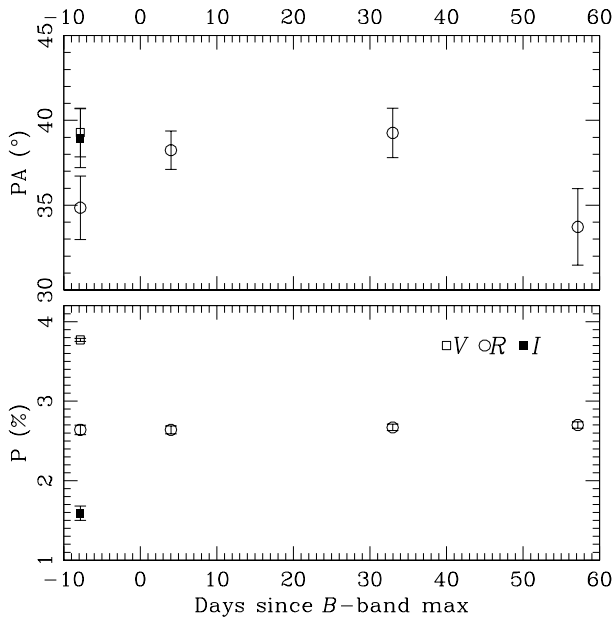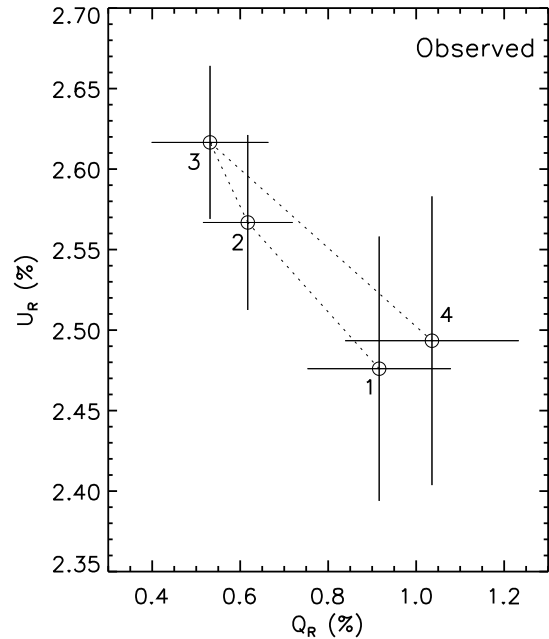

Figure 6. Observed Q-U diagram of SN 2014J in R-band. Numbers labelled with 1–4 and connected with dotted lines, indicate the temporal order.

U-band photometry is not available beyond +115d. Thus, we use only the $UBVRI$ magnitudes to estimate the quasi-bolometric fluxes between +88 to +115d, and only $BVRI$ magnitudes thereafter.

The UVOIR bolometric light curve of SN 2014J is shown in Figure 7, along with the bolometric light curves of SN 2011fe, SN 2005cf and SN 2003du. The bolometric light curves of SNe 2011fe (Richmond & Smith 2012), 2005cf (Pastorello et al. 2007) and 2003du (Anupama, Sahu & Jose 2005) were constructed using the published $UBVRI$ magnitudes. A 20 % constant contribution was added in order to account for missing flux from UV and NIR passbands for SNe 2011fe, 2005cf and 2003du.

SN 2014J reached a peak UVOIR bolometric magnitude of $M_{bol}^{max} \approx -18.9 \pm 0.20$, which is similar to the peak bolometric magnitudes of the normal SNe 2011fe, 2005cf and 2003du. The date of explosion for SN 2014J was reported to be January 14.75 UT (Zheng et al. 2014) and 14.54 UT (Goobar et al. 2015). Assuming an explosion date of 14.65 UT, which is the average of the above estimates, the rise time to maximum for SN 2014J is $\sim$ 18 days, which is consistent with those of normal SNe Ia.

The bolometric light curves of SNe Ia are powered by the decay chain ^{56}Ni $\rightarrow$ ^{56}Co $\rightarrow$ ^{56}Fe. A combination of three parameters - the mass of ^{56}Ni synthesized in the explosion (M_{Ni}), the total ejecta mass (M_{ej}) and the kinetic energy of the explosion (E_k) determines the peak luminosity and width of the bolometric light curve (Arnett 1982).

Using Arnett's rule (Arnett 1982) to estimate the mass of ^{56}Ni synthesized for a rise time $t_R \sim$ 18 days and a peak bolometric flux $L_{bol}^{max} \approx 1.06 \times 10^{43}$ erg s^{-1}, we obtain $M_{Ni} \approx 0.5$ M$_\odot$, assuming $\alpha = 1$.

In order to estimate the physical parameters of the explosion, i.e. M_{Ni}, M_{ej} and E_k, we fit the observed bolometric light curve with a simple analytical model proposed by

Figure 5. Temporal evolution of the observed polarization parameters of SN 2014J. The upper and lower panels represent the polarization angle and degree of polarization, respectively. Symbols used in both panels are same.

rapidly from $\sim$ 4% at -5d to $<$ 1% beyond +20d for SN 2014J. The diminishing UV contribution is taken into account up to $\sim$ 30 days since B-band maximum. The peak contribution from UV to the bolometric flux was found to be $\sim$ 13% for SN 2011fe (Pereira et al. 2013) and $\sim$ 19% for SN 2013dy (Pan et al. 2015), which is higher than our estimate of $\sim$ 4% for SN 2014J using HST spectra.

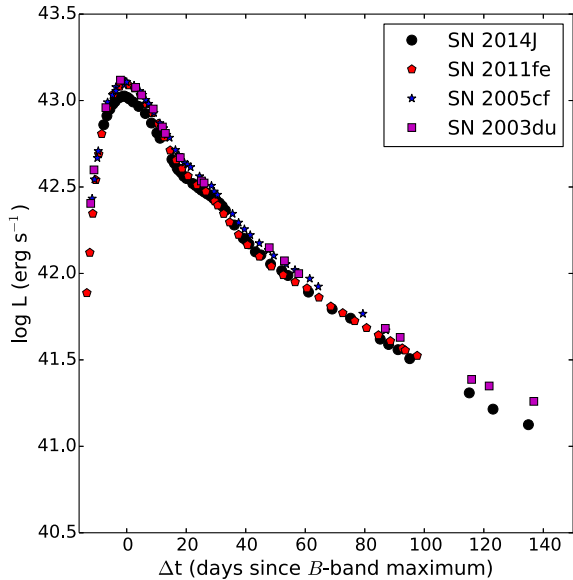JHK_s photometry is not available beyond +88d, and

Figure 7. UVOIR bolometric light curve of SN 2014J plotted along with the bolometric light curves of SN 2011fe, SN 2005cf and SN 2003du. The bolometric light curves were constructed as described in the text.
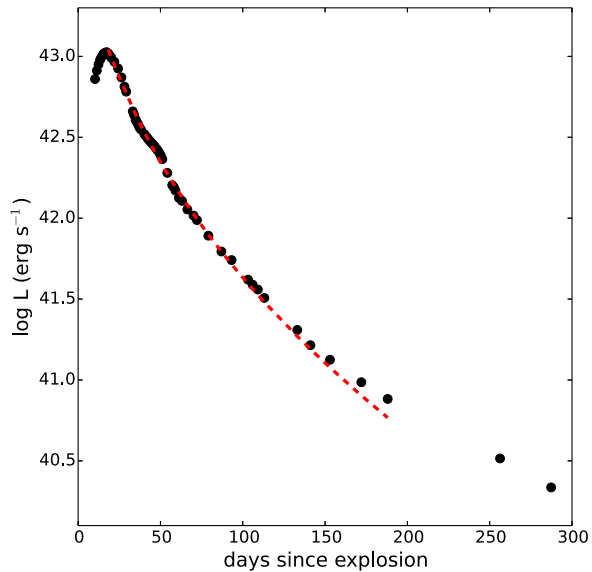

Figure 8. *UVOIR* bolometric light curve of SN 2014J plotted along with the computed model (Vinkó et al. 2004) corresponding to the best-fit parameter values.

Vinkó et al. (2004). The assumptions in the model include spherical symmetry, homologous expansion of the ejecta and a constant opacity for γ-rays and positrons. A core-shell density structure is assumed with a constant density core of fractional radius x_0, and an outer shell with density decreasing outward as a power law with exponent n.

The free parameters in the model are ejected mass (M_{ej}), nickel mass (M_{Ni}), γ-ray opacity (κ_γ), positron opacity (κ_+), ejecta expansion velocity (v_{exp}) and the density power law exponent (n).

Fitting this model to the post-maximum part of the bolometric light curve until 188 days since explosion, we obtain the following best-fit parameter values for a fixed fractional core radius ($x_0 = 0.15$):
$M_{ej} \sim 1.3$ $M_\odot$ (consistent with usual values of $0.9 - 1.4$ $M_\odot$ for SNe Ia), $M_{Ni} \sim 0.6$ $M_\odot$, $\kappa_\gamma \sim 0.03$ cm^2 g^{-1} (consistent with the usual value of 0.027 cm^2 g^{-1} for grey atmospheres), $\kappa_+ \sim 0.04$ cm^2 g^{-1}, $v_{exp} \sim 10\,000$ km s^{-1} (consistent with photospheric velocity of $\sim 12\,000$ km s^{-1} deduced from spectra) and $n \sim 0.9$. The kinetic energy of the explosion, $E_k \sim 7 \times 10^{50}$ erg.

The ^{56}Ni mass estimated above is consistent with the estimates of Churazov et al. (2014), Marion et al. (2015) and Telesco et al. (2015) for SN 2014J. Childress et al. (2015) estimate M_{ej} and M_{Ni} using [Co III] $\lambda5893$ emission feature in the nebular spectra of a sample of SNe Ia which includes SN 2014J. For SN 2014J, the estimated values are $M_{ej} \approx 1.44$ $M_\odot$ and $M_{Ni} \approx 0.84$ $M_\odot$. Scalzo et al. (2014) estimated M_{ej} and M_{Ni} for a sample of 19 normal SNe Ia by modelling their bolometric light curves and obtained a distribution of $0.9 < M_{ej} < 1.4$ $M_\odot$ and $M_{Ni}(avg) \sim 0.5$ $M_\odot$.

6 SPECTROSCOPY RESULTS

Optical spectra of SN 2014J were obtained on 23 epochs between -7.7d to $+351.1$d relative to B-band maximum, whereas NIR spectra were obtained on 4 epochs around B-band maximum. The optical spectra of SN 2014J show a red continuum owing to the large amount of extinction suffered by the SN, but the spectral features are essentially those of a normal SN Ia.

6.1 Spectral Evolution and SYN++ fits

The photospheric phase spectra of SN 2014J show prominent features attributable to Si II, S II, Ca II, Fe II and Mg II (eg. Goobar et al. 2014). The similarity of the early spectra of SN 2014J to SN 2011fe has been noted by Zheng et al. (2014); Goobar et al. (2014); Marion et al. (2015). However, unlike SN 2011fe, SN 2014J shows the presence of high velocity features (HVFs) in pre-maximum spectra and lacks the C II $\lambda6580$ feature, which was detected in SN 2005cf and SN 2011fe (Zheng et al. 2014; Goobar et al. 2014). The lack of detection of C II in the optical spectra could be due to the rather late discovery of SN 2014J. The earliest spectrum reported on January 22.3 UT (Goobar et al. 2014) corresponds to a phase of ~ -9d relative to B_{max}. Detection of C II becomes difficult at this phase, since the ionized carbon layer begins to cool and recombine to form C I. This does not rule out the presence of carbon in the spectra however, as pointed out by Marion et al. (2015), who report the detection of the C I 1.06 μm feature in their early NIR spectra from -7.4d to $+3.2$d.

The early spectral evolution of SN 2014J in the optical (-7.7d to $+25.2$d) and NIR (-2.8d to $+11.2$d) is shown in Figure 9 and Figure 10, respectively. The photospheric ve-
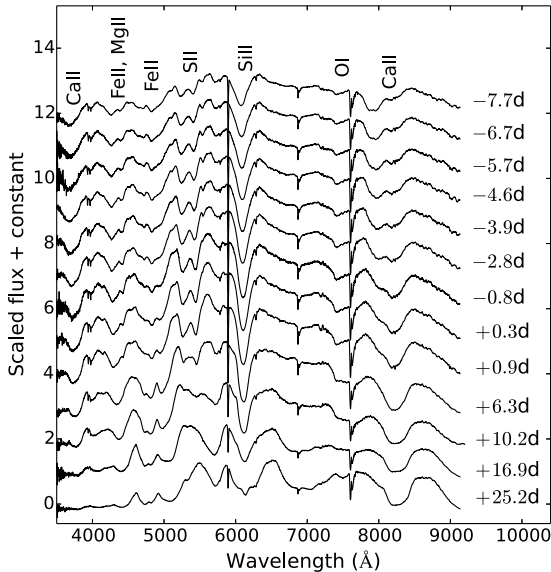
Figure 9. Early spectral evolution of SN 2014J between -7.7d to $+25.2$d. Reddening correction has not been applied to the spectra.

Figure 10. Early NIR spectral evolution of SN 2014J between -2.8d to $+11.2$d.

locity of the ejecta, as measured from the blueshift of the Si II $\lambda6355$ absorption feature, evolves from $\sim 13\,300$ km s^{-1} at -7.7d to $\sim 12\,000$ km s^{-1} near B_{max} and further falls to $\sim 11\,400$ km s^{-1} at $+17.0$d, consistent with the measurements reported by Marion et al. (2015). This places SN 2014J at the border of the normal velocity (NV) group and high velocity (HV) group of SNe Ia (Wang et al. 2009a). Our earliest optical spectrum (-7.7d) shows HV features of Ca II detached at $\sim 24\,000$ km s^{-1}, but this feature disappears rapidly as the epoch of B-band maximum approaches. The earliest NIR spectrum presented here (-2.8d) exhibits a prominent Mg II 1.09 μm feature blueshifted at $\sim 13\,000$ km s^{-1}, whereas later NIR spectra are dominated by blended absorption due to Mg II 1.68 μm, Si II 1.69 μm features (Marion et al. 2015).

The spectral evolution of SN 2014J between $\sim 1-2$ months since B_{max} is presented in Figure 11. The Si II $\lambda6355$ feature has more or less disappeared by $+32$d, and the spectra are progressively dominated by forbidden emission lines of [Fe II] and [Fe III]. Other prominent features include the Na I D lines and the Ca II NIR triplet, which persists as a strong feature even at much later phases.

As the supernova enters the nebular phase, the ejecta becomes optically thin and transparent to optical photons, thus exposing the Fe-rich core. The nebular phase spectra of SN 2014J, from a phase of $+88$d to $+351$d are shown in Figures 15, 16 and 17. The $+88$d spectrum of SN 2014J is dominated by nebular emission features of [Fe III] $\lambda4701$, [Fe II] $\lambda5159,5261$ and Na I/[Co III] features near 5900 Å. The [Fe III] $\lambda4701$ remains the most prominent feature in the $+351$d spectrum of SN 2014J. In addition, the [Fe II] blend near 5200 Å and the [Fe II] $\lambda7155$ and [Ni II] $\lambda7378$ features are also prominent.

We fit synthetic spectra using SYN++ to the early phase, dereddened spectra of SN 2014J. SYN++ is the
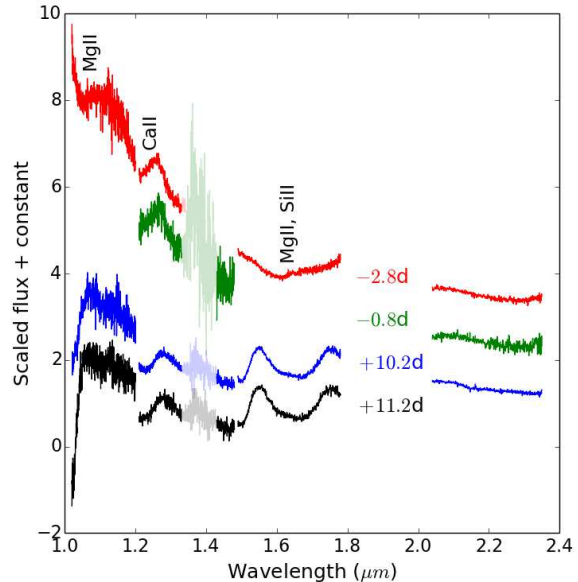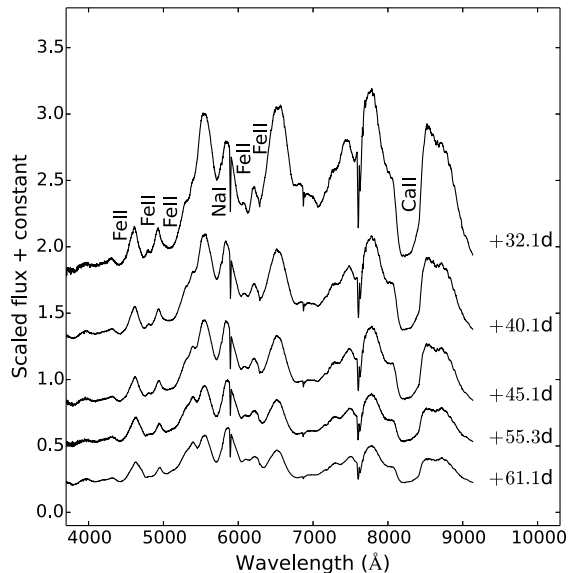

Figure 11. Spectral evolution of SN 2014J between $+32.1$d to $+61.1$d. Reddening correction has not been applied to the spectra.

rewrite of the SYNOW code in modern C++ (Fisher 2000; Thomas, Nugent & Meza 2011). The earliest spectrum obtained on -7.7d is fit with a photospheric velocity $v_{phot} = 15\,000$ km s^{-1} and a blackbody temperature $T_{bb} = 13\,500$ K. The broad Ca II NIR triplet is fit with two components – a photospheric component and a HV component detached at $24\,000$ km s^{-1}. The -2.8d spectrum is fit with the Ca II HV component at a reduced velocity of $20\,000$ km s^{-1}. The HV feature is not seen in the spectra obtained beyond the
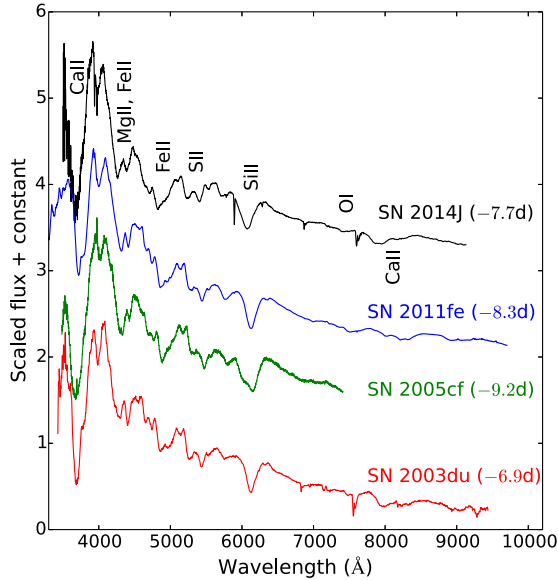
Figure 13. Dereddened −7.7d spectrum of SN 2014J plotted with spectra of SN 2011fe, SN 2005cf and SN 2003du at similar epochs for comparison.
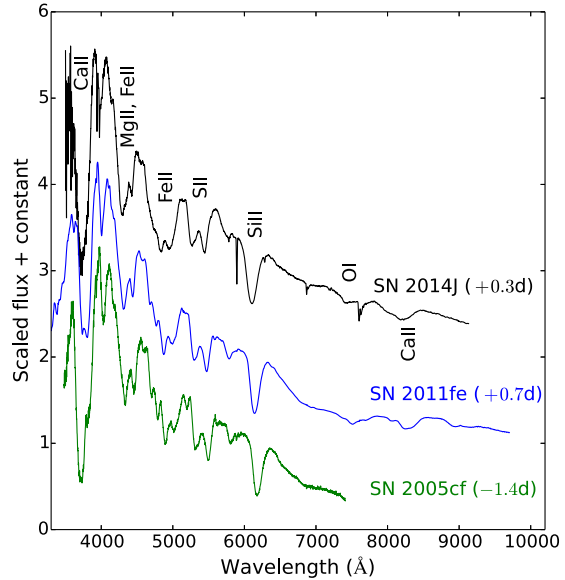

Figure 14. Dereddened spectrum of SN 2014J near epoch of B-band maximum plotted with spectra of SN 2011fe, SN 2005cf and SN 2003du at similar epochs for comparison.
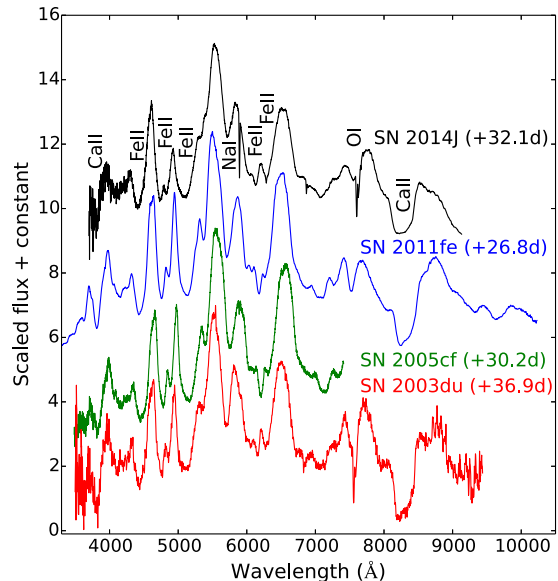
epoch of B-band maximum. The photospheric velocity decreases from $\sim 15\,000$ km s^{-1} at $−7.7$d to $\sim 12\,000$ km s^{-1} at $−2.8$d and falls to $\sim 9\,000$ km s^{-1} at $+25.2$d, whereas the blackbody temperature first increases slightly to $13\,800$ K at $−2.8$d and subsequently falls to $9\,000$ K at $+25.2$d.

Figure 12 shows the SYN++ fits obtained for the $−7.7$, $−2.8$, $+10.3$ and $+25.2$d spectra of SN 2014J.

6.2   Comparison with normal SNe Ia

Since SN 2014J has suffered significant reddening in its host environment, all the spectra of SN 2014J shown here have been dereddened with $E(B − V) = 1.24$ and $R_V = 1.44$ (Foley et al. 2014) for comparison with SNe 2011fe, 2005cf and 2003du. Figure 13 shows our earliest spectrum ($−7.7$d) of SN 2014J, plotted along with spectra of SN 2011fe (Pereira et al. 2013), SN 2005cf (Wang et al. 2009b) and SN 2003du (Anupama, Sahu & Jose 2005) for comparison. The spectra are quite similar, except for the fact that SN 2005cf shows a prominent HV component in the Si II $\lambda6355$ feature, unlike the other SNe.

Figure 14 shows spectrum of SN 2014J near the epoch of B-band maximum, compared to SNe 2011fe and 2005cf. Again, the spectra are very similar to each other but the features of SN 2014J show a higher blueshift, indicating higher expansion velocities. The spectra of SN 2011fe and SN 2005cf used for comparison were downloaded from the WISeREP archive[4] (Yaron & Gal-Yam 2012).

Figure 15 shows the $+32.1$d spectrum of SN 2014J, along with spectra of SN 2011fe (Mazzali et al. 2014), SN 2005cf (Wang et al. 2009b) and SN 2003du (Anupama, Sahu & Jose 2005) at similar epochs.

Figure 15. Dereddened $+32.1$d spectrum of SN 2014J, plotted with spectra of SN 2011fe, SN 2005cf and SN 2003du at similar epochs.

Figure 16 shows the $+88$d spectrum of SN 2014J, along with the spectra of SNe 2011fe, 2005cf and 2003du for comparison. The spectra of all the SNe are remarkably similar during this early nebular phase. In Figure 17, we compare nebular spectra of SN 2014J at $+154$d with those of SN 2011fe (Mazzali et al. 2015) and SN 2003du, whereas in Figure 18, we compare the $+269$d and $+351$d spectra of SN
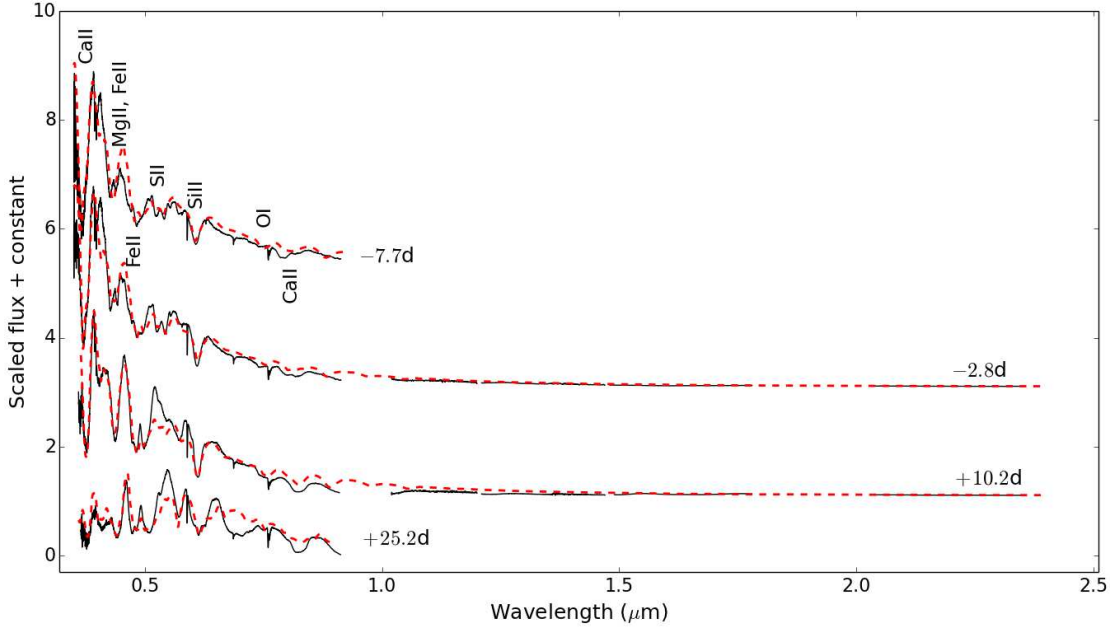
Figure 12. Dereddened spectra of SN 2014J near the epoch of maximum light plotted along with synthetic spectra generated using SYN++ (dashed lines). The full optical/NIR fit is shown for the -2.8d and $+10.2$d spectra.

2014J with those of SN 2011fe (Mazzali et al. 2015) obtained at similar epochs. The spectral evolution of SN 2014J is remarkably similar to SN 2011fe till ~ 150 days. However, their spectra show small differences at later phases, as seen in Figure 18. The relative strengths of the [Fe III] $\lambda 4701$ feature and [Fe II] $\lambda 5200$ blend in the nebular spectra is a measure of the ionization state of the ejecta. A lower ratio of [Fe III]/[Fe II] indicates clumpiness in the ejecta (Mazzali et al. 2001). The $+351$d spectrum of SN 2014J shows a [Fe III]/[Fe II] ratio of 0.89, whereas the same ratio for the $+345$d spectrum of SN 2011fe is 1.33. The relatively low [Fe III]/[Fe II] ratio thus hints towards a clumpy ejecta for SN 2014J.

We measure the velocity of the nebular emission features of SN 2014J, namely [Fe III] $\lambda 4701$, [Fe II] $\lambda 7155$ and [Ni II] $\lambda 7378$. The [Fe III] $\lambda 4701$ feature evolves from a velocity of ~ -3700 km s^{-1} at $+88$d, to ~ -1700 km s^{-1} at $+351$d. The [Fe II] $\lambda 7155$ and [Ni II] $\lambda 7378$ features show a redshift of ~ 1000 and ~ 1600 km s^{-1} respectively at $+351$d, unlike SN 2011fe where these nebular features are blueshifted, as noted by Lundqvist et al. (2015).

6.3 Spectroscopic Properties

Figure 19 shows the velocity evolution of Si II $\lambda 6355$ feature in SN 2014J during the early phase, along with the velocity evolution of SN 2007co (Blondin et al. 2012), SN 2005cf (Pastorello et al. 2007), SN 2003du (Anupama, Sahu & Jose 2005) and SN 2002bo (Benetti et al. 2004). The velocity evolution of SN 2014J in the pre-maximum phase is similar to the normal type Ia SN 2007co (Foley & Kasen 2011; Blondin et al. 2012).

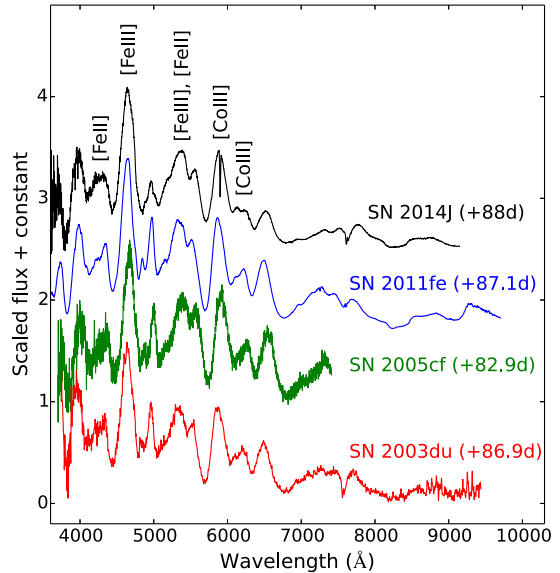Based on the photospheric velocity deduced from the

Figure 16. Dereddened $+88$d spectrum of SN 2014J, plotted along with spectra of SNe 2011fe, 2005cf and 2003du at similar epochs.

Si II $\lambda 6355$ feature near the epoch of B-band maximum, Wang et al. (2009a) classified SNe Ia as normal velocity (NV) or high velocity (HV) objects, where HV objects show a velocity $v_{phot} \gtrsim 11\,800$ km s^{-1}. Fitting a spline function to the velocity points close to maximum, we estimate $v_{phot}(B_{max}) \approx 12\,000$ km s^{-1} for SN 2014J, in agreement
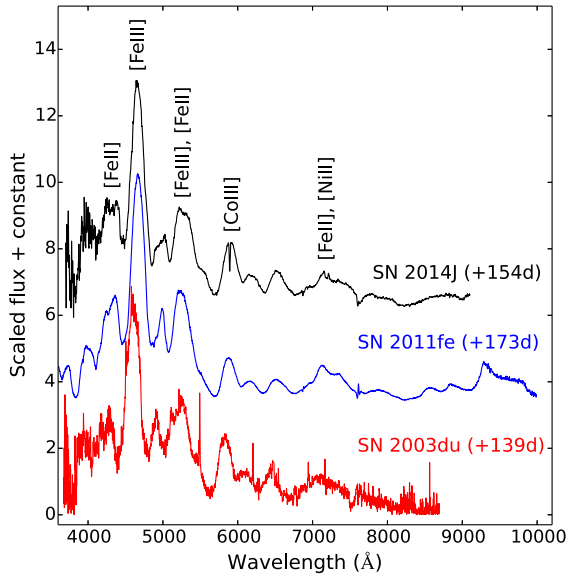
Figure 17. Dereddened +154d nebular spectrum of SN 2014J, plotted along with spectra of SNe 2011fe and 2003du at similar epochs.

Figure 19. Velocity evolution of Si II 6355 Å feature for SN 2014J, along with a few other SNe Ia for comparison.
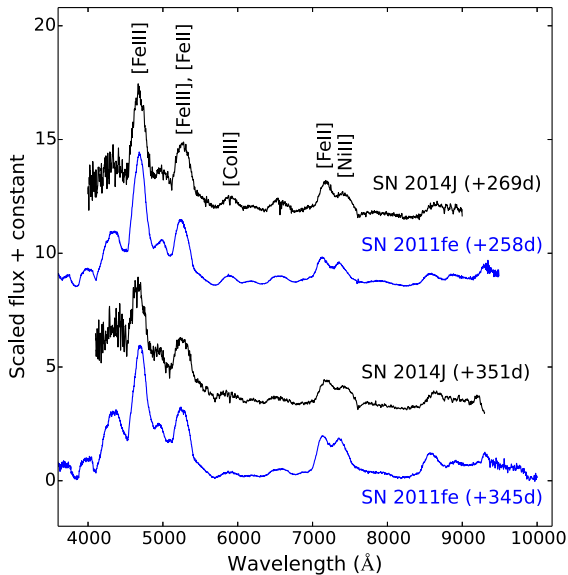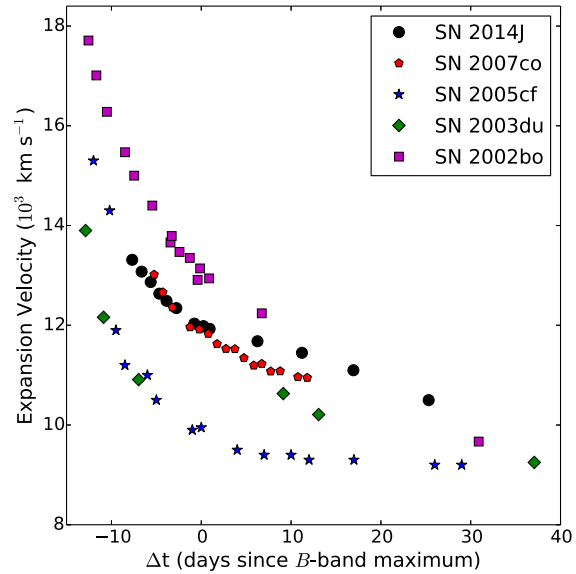

Figure 18. Dereddened nebular spectra of SN 2014J at +269d and +351d, plotted along with nebular spectra of SN 2011fe at similar epochs for comparison.

with Marion et al. (2015). According to the classification scheme of Wang et al. (2009a), this places SN 2014J at the border of the HV and NV group of SNe Ia.

Benetti et al. (2005) categorized SNe Ia on the basis of the velocity gradient of the Si II $\lambda6355$ feature ($\dot{v}_{Si}$) around the epoch of B-band maximum. Those events showing high

velocity gradients ($\dot{v}_{Si} \gtrsim 70$ km s^{-1} day^{-1}) are termed as HVG, whereas the ones showing slow velocity evolution are termed as LVG. A third group of SNe Ia, which show low velocities but a rapid temporal velocity evolution, are categorized as FAINT. The FAINT subclass contains sub-luminous events like SN 1991bg. The HVG comprises of normal events, while the LVG subclass contains both normal and luminous 1991T-like events. Figure 20 shows where SN 2014J fits in with other SNe Ia according to the Benetti et al. (2005) scheme. The velocity gradient calculated for SN 2014J between +0 and +10d since B-band maximum, $\dot{v}_{Si} \approx 50$ km s^{-1} day^{-1}. As pointed out by Marion et al. (2015), the measured velocity gradient places SN 2014J in the LVG group of SNe Ia, but not far from the boundary of HVG and LVG events. SNe 2003du and 2005cf also belong to the LVG subclass, whereas SN 2002bo lies in the HVG group, showing high velocities and a rapid velocity evolution. The velocity of SN 2007co matches well with SN 2014J in the pre-maximum phase, but falls off faster post maximum. With a velocity gradient $\dot{v}_{Si} \approx 90$ km s^{-1}, SN 2007co lies in the HVG subclass. The velocities of SN 2007co (Blondin et al. 2012) were estimated from its spectra obtained from WISeREP.

Branch et al. (2006) provide an alternative method of classifying SNe Ia based on their spectra. The ratio of the pseudo-Equivalent Widths (pEW) of Si II $\lambda5972$ and $\lambda6355$ features in spectra near the epoch of B-band maximum forms four regions or clusters - namely core normal (CN), shallow silicon (SS), broad line (BL) and cool (CL). For the +0.3d spectrum of SN 2014J, we measure pEW($\lambda5972$) ≈ 14.5 and pEW($\lambda6355$) ≈ 108.9. According to the Branch et al. (2006) scheme, SN 2014J lies on the border of the CN and BL subclasses of SNe Ia (Figure 21). SN 2007co was classified as a BL object (Blondin et al. 2012) and lies close to SN 2014J in the Branch et al. (2006) scheme, as seen in Figure 21.
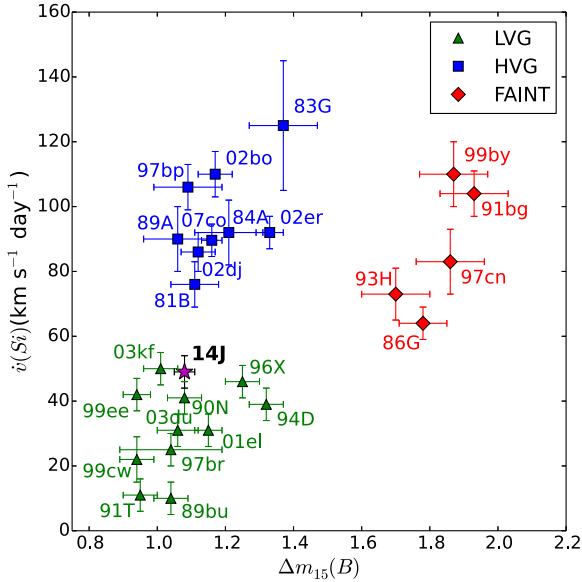
Figure 20. Spectroscopic classification of SN 2014J according to Benetti et al. (2005) scheme. The sample of SNe Ia have been taken from Benetti et al. (2005) and Blondin et al. (2012). The position of SN 2014J is marked by the filled ★.
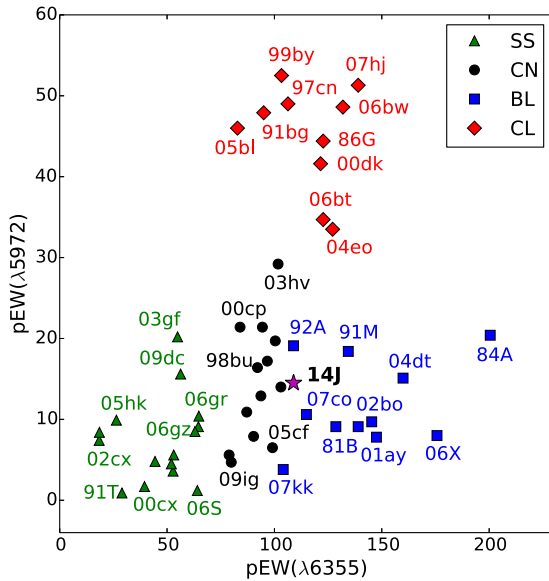

Figure 21. Spectroscopic classification of SN 2014J according to Branch et al. (2006) scheme using pEWs of Si II features. The sample of SNe Ia is taken from Branch et al. (2006); Blondin et al. (2012) and Pereira et al. (2013). The position of SN 2014J is marked by the filled ★.

7 SUMMARY AND CONCLUSION

We present photometric and spectroscopic observations of SN 2014J, spanning -8 to $+269$d and $+351$d since B-band maximum, respectively. For a host galaxy reddening of $E(B - V) \approx 1.24$ with $R_V \approx 1.44$ (Foley et al. 2014), in addition to a Galactic foreground reddening of $E(B - V)_{MW} \approx 0.05$, the peak V-band magnitude, $M_V(max) \approx -19.20 \pm 0.20$. The light curves show a normal decline rate of $\Delta m_{15}(B) \approx 1.08 \pm 0.03$. Fitting a simple analytical model to the bolometric light curve provides estimates of $M_{ej} \sim 1.3$ $M_\odot$, $M_{Ni} \sim 0.6$ $M_\odot$ and $E_k \sim 7 \times 10^{50}$ erg.

The velocity evolution of SN 2014J, with a Si II $\lambda 6355$ velocity of $\sim 12\,000$ km s^{-1} at B-band maximum, places it in the LVG subclass; whereas the pEW measurements of Si II $\lambda 5972, \lambda 6355$ features place SN 2014J at the boundary of CN and BL subclasses of SNe Ia. SN 2014J shows redshifted nebular emission features of [Fe II] $\lambda 7155$ (~ 1000 km s^{-1}) and [Ni II] $\lambda 7378$ (~ 1600 km s^{-1}) at $+351$d, as noted by Lundqvist et al. (2015). The low ratio of [Fe III]/[Fe II] in the nebular spectra of SN 2014J indicates a lower degree of ionization in SN 2014J, which points towards a clumpy ejecta.

REFERENCES

Amanullah R. et al., 2014, ApJL, 788, L21
Anupama G. C., Sahu D. K., Jose J., 2005, A & A, 429, 667
Arnett W. D., 1982, ApJ, 253, 785
Ashall C., Mazzali P., Bersier D., Hachinger S., Phillips M., Percival S., James P., Maguire K., 2014, MNRAS, 445, 4427
Benetti S. et al., 2005, ApJ, 623, 1011
Benetti S. et al., 2004, MNRAS, 348, 261
Bessell M. S., Castelli F., Plez B., 1998, A & A, 333, 231
Blondin S. et al., 2012, AJ, 143, 126
Branch D. et al., 2006, PASP, 118, 560
Brown P. J. et al., 2015, ApJ, 805, 74
Cardelli J. A., Clayton G. C., Mathis J. S., 1989, ApJ, 345, 245
Childress M. J. et al., 2015, MNRAS, 454, 3816
Chornock R., Filippenko A. V., Branch D., Foley R. J., Jha S., Li W., 2006, PASP, 118, 722

Churazov E. et al., 2014, Nature, 512, 406

Crotts A. P. S., 2015, ApJL, 804, L37

Diehl R. et al., 2014, Science, 345, 1162

Diehl R. et al., 2015, A & A, 574, A72

Elias-Rosa N. et al., 2006, MNRAS, 369, 1880

Elias-Rosa N. et al., 2008, MNRAS, 384, 107

Eswaraiah C., Pandey A. K., Maheswar G., Chen W. P., Ojha D. K., Chandola H. C., 2012, MNRAS, 419, 2587

Eswaraiah C., Pandey A. K., Maheswar G., Medhi B. J., Pandey J. C., Ojha D. K., Chen W. P., 2011, MNRAS, 411, 1418

Filippenko A. V., 1997, ARA & A, 35, 309

Fisher A. K., 2000, PhD thesis, THE UNIVERSITY OF OKLAHOMA

Foley R. J. et al., 2014, MNRAS, 443, 2887

Foley R. J., Kasen D., 2011, ApJ, 729, 55

Fossey J., Cooke B., Pollack G., Wilde M., Wright T., 2014, Central Bureau Electronic Telegrams, 3792, 1

Gao J., Jiang B. W., Li A., Li J., Wang X., 2015, ApJL, 807, L26

Goobar A., 2008, ApJL, 686, L103

Goobar A. et al., 2014, ApJL, 784, L12

Goobar A. et al., 2015, ApJ, 799, 106

Greaves J. S., Holland W. S., Jenness T., Hawarden T. G., 2000, Nature, 404, 732

Hoyle F., Fowler W. A., 1960, ApJ, 132, 565

Iben, Jr. I., Tutukov A. V., 1984, ApJS, 54, 335

Jack D. et al., 2015, MNRAS, 451, 4104

Kawabata K. S. et al., 2014, ApJL, 795, L4

Kelly P. L. et al., 2014, ApJ, 790, 3

Krisciunas K., Prieto J. L., Garnavich P. M., Riley J.-L. G., Rest A., Stubbs C., McMillan R., 2006, AJ, 131, 1639

Kumar B., Pandey S. B., Eswaraiah C., Gorosabel J., 2014, MNRAS, 442, 2

Landolt A. U., 1992, AJ, 104, 340

Leonard D. C., Li W., Filippenko A. V., Foley R. J., Chornock R., 2005, ApJ, 632, 450

Li W. et al., 2011, MNRAS, 412, 1441

Lundqvist P. et al., 2015, A & A, 577, A39

Maeda K., Nozawa T., Nagao T., Motohara K., 2015, MNRAS, 452, 3281

Maoz D., Mannucci F., Nelemans G., 2014, ARA & A, 52, 107

Margutti R., Parrent J., Kamble A., Soderberg A. M., Foley R. J., Milisavljevic D., Drout M. R., Kirshner R., 2014, ApJ, 790, 52

Marion G. H. et al., 2015, ApJ, 798, 39

Maund J. R. et al., 2013, MNRAS, 433, L20

Mazzali P. A., Nomoto K., Patat F., Maeda K., 2001, ApJ, 559, 1047

Mazzali P. A. et al., 2015, MNRAS, 450, 2631

Mazzali P. A. et al., 2014, MNRAS, 439, 1959

Ninan J. P. et al., 2014, Journal of Astronomical Instrumentation, 3, 50006

Nobili S., Goobar A., 2008, A & A, 487, 19

O'Donnell J. E., 1994, ApJ, 422, 158

Ojha D. K. et al., 2012, in Astronomical Society of India Conference Series, Vol. 4, p. 191

Pan Y.-C. et al., 2015, MNRAS, 452, 4307

Pandey J. C., Medhi B. J., Sagar R., Pandey A. K., 2009, MNRAS, 396, 1004

Pastorello A. et al., 2007, MNRAS, 376, 1301

Patat F., Baade D., Höflich P., Maund J. R., Wang L., Wheeler J. C., 2009, A & A, 508, 229

Patat F. et al., 2013, A & A, 549, A62

Patat F. et al., 2015, A & A, 577, A53

Pereira R. et al., 2013, A & A, 554, A27

Pérez-Torres M. A. et al., 2014, ApJ, 792, 38

Perlmutter S. et al., 1999, ApJ, 517, 565

Phillips M. M., Lira P., Suntzeff N. B., Schommer R. A., Hamuy M., Maza J., 1999, AJ, 118, 1766

Phillips M. M. et al., 2013, ApJ, 779, 38

Ramaprakash A. N., Gupta R., Sen A. K., Tandon S. N., 1998, A&AS, 128, 369

Rautela B. S., Joshi G. C., Pandey J. C., 2004, Bulletin of the Astronomical Society of India, 32, 159

Richmond M. W., Smith H. A., 2012, Journal of the American Association of Variable Star Observers (JAAVSO), 40, 872

Riess A. G. et al., 1998, AJ, 116, 1009

Ritchey A. M., Welty D. E., Dahlstrom J. A., York D. G., 2015, ApJ, 799, 197

Scalzo R. et al., 2014, MNRAS, 440, 1498

Schmidt G. D., Elston R., Lupie O. L., 1992, AJ, 104, 1563

Smith P. S., Williams G. G., Smith N., Milne P. A., Jannuzi B. T., Green E. M., 2011, ArXiv:1111.6626

Stalin C. S., Hegde M., Sahu D. K., Parihar P. S., Anupama G. C., Bhatt B. C., Prabhu T. P., 2008, Bulletin of the Astronomical Society of India, 36, 111

Telesco C. M. et al., 2015, ApJ, 798, 93

Thomas R. C., Nugent P. E., Meza J. C., 2011, PASP, 123, 237

Tsvetkov D. Y., Metlov V. G., Shugarov S. Y., Tarasova T. N., Pavlyuk N. N., 2014, Contributions of the Astronomical Observatory Skalnate Pleso, 44, 67

Vinkó J. et al., 2004, A & A, 427, 453

Wang L. et al., 2003, ApJ, 591, 1110

Wang L., Baade D., Höflich P., Wheeler J. C., Kawabata K., Khokhlov A., Nomoto K., Patat F., 2006, ApJ, 653, 490

Wang L., Wheeler J. C., 2008, ARA & A, 46, 433

Wang L., Wheeler J. C., Höflich P., 1997, ApJL, 476, L27

Wang X. et al., 2009a, ApJL, 699, L139

Wang X. et al., 2009b, ApJ, 697, 380

Wang X. et al., 2008, ApJ, 675, 626

Webbink R. F., 1984, ApJ, 277, 355

Whelan J., Iben, Jr. I., 1973, ApJ, 186, 1007

Woosley S. E., Weaver T. A., 1986, ARA & A, 24, 205

Yaron O., Gal-Yam A., 2012, PASP, 124, 668

Zelaya P. et al., 2013, AJ, 145, 27

Zheng W. et al., 2014, ApJL, 783, L24

APPENDIX A: TEMPLATE SUBTRACTION

Pre-explosion SDSS *ugriz* images of M82 were used in order to subtract the underlying host galaxy contribution at later phases ($\gtrsim$ 60 days since B-band maximum) to obtain accurate magnitudes of SN 2014J. The SDSS images were first aligned and spatially rescaled to match the $BVRI$ images of SN 2014J. The *ugriz* images were then converted from counts scale to magnitude scale using $Image_{mag} = -2.5 \times log(Image_{counts})$. Subsequently, the *ugriz* images (in magnitude scale) were arithmetically

transformed as prescribed by the Lupton formulae (Lupton 2005) to obtain equivalent $BVRI$ images in the magnitude scale, which were converted back to the counts scale. The equivalent $BVRI$ images thus obtained were used for the template subtraction.

To check the accuracy of the transformations, aperture photometry was performed on the SDSS $ugriz$ images for a small galaxy region centered around the SN location and the $ugriz$ magnitudes were calculated, which were then transformed to $BVRI$ magnitudes using the Lupton formulae. Next, aperture photometry was performed for the same region with the same aperture for the equivalent $BVRI$ images obtained by performing the pixel to pixel transformation described above. The magnitudes derived by the two methods were seen to match within 0.01 mag. The same test was performed on a couple of stars in the field and the magnitudes were seen to agree within 0.02 mag.